Radiation damage in ion-irradiated CeO_2 and (Ce, Gd)O_2 sinters: effect of the Gd content

Jean-Marc Costantini, Gaëlle Gutierrez, Gérald Lelong, Maxime Guillaumet, Pooreun Seo, Kazuhiro Yasuda

RADIATION DAMAGE IN ION-IRRADIATED CeO_2 AND (Ce, Gd)O_2 SINTERS: EFFECT OF THE Gd CONTENT

Jean-Marc COSTANTINI[1],

Université Paris-Saclay, CEA, Service de Recherches Métallurgiques Appliquées, 91191, Gif-sur Yvette, France

Gaëlle GUTTIEREZ,

Université Paris-Saclay, CEA, Service de Recherches de Métallurgie Physique, 91191, Gif-sur-Yvette, France

Gérald LELONG, Maxime GUILLAUMET,

Sorbonne Université, Muséum National d'Histoire Naturelle, UMR CNRS 7590, IRD, Institut de Minéralogie, de Physique des Matériaux et de Cosmochimie, IMPMC, 75005 Paris, France

Pooreun SEO, and Kazuhiro YASUDA,

Department of Applied Quantum Physics and Nuclear Engineering, Kyushu University, 744 Motooka, Nishi-ku, Fukuoka, 819-0395 Japan

ABSTRACT

The radiation damage induced in cerium dioxide CeO_2 and cerium-gadolinium mixed oxides (Ce, Gd)O_{2-x} was studied by micro-Raman spectroscopy and diffuse UV-visible reflectance spectroscopy. Sintered samples of undoped CeO_2 and (Ce, Gd)O_{2-x} for 1 mol% and 5 mol% of Gd_2O_3 were irradiated at room temperature with 2.5-MeV Ar^{2+} and 12-MeV Ar^{4+} ions up to high fluences (i.e. $5x10^{14}$ cm^{-2} and $2.1x10^{14}$ cm^{-2} respectively). The Raman spectra show that no amorphization of those oxides occurs whatsoever, regardless of the Gd content. However, the damage cross section deduced from the decay of F_{2g} peak intensity versus fluence seems to decrease with the Gd^{3+} content. Moreover, the reflectivity spectra show a clear decrease of the band-gap energy and increase of the Urbach energy arising from point defect accumulation. Similar effects are found for 1 mol% and 5 mol% Gd_2O_3, whereas a larger effect on band tailing is seen for undoped ceria. The respective roles of nuclear collisions and electronic excitations are discussed for both ion energies knowing that the two kinds of measurements do not probe the same sample depth. The substitution of Gd^{3+} ions for Ce^{4+} ions is likely reducing the damage and the formation of band tails related to the formation of Ce^{3+} ions by electronic excitation processes.

Keywords: Cerium-gadolinium oxides, heavy ion irradiation, diffuse reflectivity, Raman spectroscopy.

[1] Corresponding author's email : jean-marc.costantini@cea.fr

I. INTRODUCTION

Cerium dioxide (CeO_2) or ceria is envisioned as a potential solid oxide fuel cell (SOFC) and solid oxide electrolysis cell (SOEC) material, for use as an electrode or electrolyte in power units operating at high-temperatures, or for catalytic applications [*Sun, 2012; Coduri, 2018; Schmitt, 2020*]. Ceria is also an important material for the nuclear applications since it is considered as a surrogate of the actinide dioxides with the same cubic fluorite-like structure such as PuO_2 [*Weber, 1984*]: Ce is sharing the same 3+ and 4+ oxidation states as Pu [*Eyring, 1967; Petit, 2010*]. Actually, both the sesquioxide (Pu_2O_3) and dioxide (PuO_2) exist in the Pu-O phase diagram like in the Ce-O phase diagram [*Adachi, 1998; Petit, 2010*]. Furthermore, the 5f electrons become more localized starting with Pu in the actinide series [*Vitova, 2017*], just like the 4f electrons in the lanthanide series in the normal conditions [*Eyring, 1967*]. Moreover, similar point defect properties are found for CeO_2 and UO_2 [*Shi, 2012*].

The behavior of ceria under irradiation is quite peculiar since it is a radiation-resistant non-amorphizable ceramics like the other dioxides with the same cubic fluorite-like structure, such as UO_2 [*Matzke, 1996*] or ZrO_2: Y [*Costantini, 2013*]. Several experimental techniques were used for probing the radiation damage at different length scales in undoped CeO_2, such as X-ray Diffraction (XRD) [*Ishikawa, 2012*; *Tracy, 2015*], X-ray absorption spectroscopy (XAS/EXAFS) [*Tracy, 2015*], transmission electron microscopy (TEM) [*Sonoda, 2006*], Raman spectroscopy [*Costantini 2017, 2019a, Graham, 2018*], scanning transmission electron microscopy (STEM) [*Takaki, 2016*], UV-visible absorption spectroscopy [*Costantini, 2016*], and diffuse reflection spectroscopy [*Costantini, 2019b*], cathodo-luminescence (CL) spectroscopy [*Costantini, 2020*], and electron-paramagnetic resonance (EPR) spectroscopy [*Costantini 2018*]. In this respect, the study of the atomic disorder at different length scales is an important issue for such a non-amorphizable material.

The reduction of Ce^{4+} ($4f^0$) to Ce^{3+} ($4f^1$) was evidenced by EPR and CL after electron irradiation due to elastic collisions [*Costantini, 2016, 2020*] or after heavy ion irradiation by UV-visible optical reflectivity due to electronic excitations [*Costantini, 2019b*]. The analysis of emission and absorption spectra suggested that Ce^{3+} is associated to oxygen vacancies in dimer or trimer defect clusters in accordance with point defect calculations [*Keating, 2012; Zacherle, 2013, Schmitt, 2020*]. A similar reduction effect is quite likely for PuO_2 under irradiation. The more complex behavior of UO_2 is fairly unknown for the 4+, 5+ and 6+ oxidation states of U in the oxides [*Kvashnina, 2013*]. Even more complex is the case of (U, Pu)O_2 or (U, Gd)O_2 fuels upon in-pile displacement damage by neutron irradiation and electronic excitations induced by fission fragments [*Devanathan, 2010*].

In view to address such effects on oxidation state evolution in mixed oxides upon irradiation, we have started the study of (Ce, RE^{3+})O_{2-x} mixed oxides with trivalent rare earth elements (RE) such as ($Ce_{1-y}Gd_yO_{2-y/2}$). The Gd^{3+} ions ($4f^7$) are substituted for Ce^{4+} ions thereby generating oxygen

vacancies ($V_O^{\cdot\cdot}$) with the 2+ charge state by charge compensation of the Gd^{3+} ions (Gd_{Ce}') [*Minervini, 1999; Nakayama, 2009*] (using the Kröger-Vink notation). As a result, the Gd-doped ceria shows a very high ionic conductivity above ~500°C [*Coduri, 2018*]. Unlike for undoped CeO_2, the oxygen deficiency in (Ce, Gd)O_{2-x} is mainly fixed by the Gd_2O_3 content [*Mogensen, 2000; Coduri, 2018; Schmitt, 2020*]. It is a general concern that irradiation of oxides under vacuum may lead to in-beam uncontrolled deviations to stoichiometry. Moreover, the case of Gd^{3+} ions in (Ce, Gd)O_{2-x} is simpler since there is little difference in the Shannon ionic radius (1.053 Å) with Ce^{4+} ions (0.97 Å) in the eightfold coordination [*Ohashi, 1998*] in contrast to other trivalent RE ions such as Nd^{3+} with a larger ionic radius (1.109 Å) [*Shannon, 1976*]. As a result, the internal lattice strain in the (Ce, Gd)O_{2-x} mixed oxides is lower than in (Ce, Nd)O_{2-x}. It is also often admitted that displacement damage is limited by the native vacancies owing to point-defect recombination such as for ZrO_2: Y [*Devanathan 2008; Costantini, 2013*]. Those are indeed good features for the study of radiation damage in the Ce–Gd–O solid solutions, as a starting point for low Gd contents, outside the miscibility gap of the two α and α' fluorite phases in the phase diagram [*Mogensen, 2000*].

Few published data are available on the radiation damage in mixed RE oxides. *Tahara et al.* have claimed that the radiation damage is enhanced in (Ce, Gd)O_{2-x} (for 1, 5, and 10 mol% Gd_2O_3) with respect to undoped CeO_2 after 200-MeV Xe^{14+} ion irradiation on the basis of XRD and XAS data [*Tahara, 2011, 2012*]. They concluded that the increase of lattice disorder near the Gd^{3+} ions is due to the lowering of lattice binding energy induced by Gd^{3+} substitution as seen from the increase of interatomic Ce-O and Ce-Ce distances deduced from the EXAFS data at the Ce L3-edge and Gd L3-edge [*Tahara, 2012*]. This is accompanied by an expansion of the unit cell with ion fluence evidenced by the XRD data [*Tahara, 2011*].

The present paper deals with the study of radiation damage and electronic structure evolution of (Ce, Gd)O_{2-x} sintered samples with a variable Gd_2O_3 content up to 5 mol% (10 Gd at%, y = 0.1) as compared to undoped CeO_2 after heavy ion irradiations for two different energies. Diffuse reflectivity in the UV-visible range and micro-Raman spectroscopy were used like for undoped CeO_2 sinters [*Costantini 2017, Costantini, 2019b*]. The optical reflectivity spectra show a clear decrease of band-gap energy and increase of Urbach energy which both derive from point defect build-up with ion fluence. A larger effect on band tailing is found for undoped CeO_2, which can be related to the formation of Ce^{3+} ions resulting from electronic excitation processes. Such a reduction seems to be impeded by the Gd^{3+} substitution. Moreover, Raman spectra show that lattice damage is decreasing with the Gd_2O_3 content which might be due to the enhanced initial disorder in the fluorite structure induced by the Gd^{3+} substitution.

II. EXPERIMENTAL PROCEDURES

Sintered polycrystalline CeO_2 and (Ce, Gd)O_{2-x} samples were used for 1 mol% and 5 mol% Gd_2O_3, i.e. 2 at% ($Ce_{0.988}Gd_{0.02}O_{1.99}$) and 10 at% Gd ($Ce_{0.9}Gd_{0.1}O_{1.95}$), respectively. Samples were 3 mm in diameter and 150 µm in thickness, with mean grain sizes of ~10 µm. Fine surface polishing was applied to all specimens. XRD $\theta-2\theta$ powder patterns with the Cu-Kα radiation were recorded for virgin samples of each batch. The variation of lattice parameter versus Gd_2O_3, content is deduced from the (111) Bragg reflection.

Irradiations were carried out with 2.5 MeV Ar^{2+} and 12-MeV Ar^{4+} ions for various fluences up to $5x10^{14}$ cm^{-2} and $2.1x10^{14}$ cm^{-2}, respectively, at the ANDROMEDE facility (IPN, Orsay) [*https://andromede.in2p3.fr/*]. The main irradiation features were computed with the SRIM-2013 code [*http://www.srim.org/*] (Table 1), such as the electronic (S_e) and nuclear stopping (S_n) powers, mean projected range (R_p) and range straggling (ΔR_p). A higher S_e/S_n ratio is found for 12-MeV Ar ions with respect to 2.5-MeV Ar ions. Moreover, the total number of Ce and O atom displacements per ion (N_d), and total displacements per ion path length (dN_d/dx) are deduced from full cascade simulations for both ion energies in CeO_2 (with a mass density of 7.215 g cm^{-3}) for ~30,000 ions, by using the threshold displacement energies of E_d (Ce) = 58 eV and E_d(O) = 35 eV [*Yasunaga, 2008*].

Depth profiles of the electronic stopping power and nuclear-collision damage profiles in CeO_2 are deduced from the simulations for both ion energies (Fig. 1). The damage peak is lying at ~3.2 µm below the target surface for 12-MeV Ar ions and at ~1.2 µm for 2.5-MeV Ar ions. An almost equal number of displacements is obtained for Ce and O atoms, despite the different E_d values, with similar values of the total number of vacancies for both ion energies (Table 1).

UV-visible measurements were conducted in the diffuse reflection mode using a Praying Mantis™ Diffuse Reflection accessory mounted on a Perkin-Elmer Lambda-1050® spectrometer. Spectra were recorded from 200 nm to 800 nm at RT for virgin and irradiated samples with a focal spot of ~1 mm averaging the collected light over ~100 grains. Teflon was used as the blank reference. The skin depth probed by the reflectivity spectra is as large as the sample thickness owing to the low electrical conductivity of the samples at RT [*Costantini, 2019b*].

Micro-Raman spectra were recorded at RT with a 532-nm Nd-YAG laser excitation in the backscattering geometry using an Invia Reflex® Renishaw spectrometer coupled with an Olympus microscope containing an *x-y-z* stage. The TO/LO peak of a silicon wafer was used as a reference spectrum. Spectra were collected between 100 and 1100 cm^{-1} for virgin and irradiated samples with a focal spot of 1 x 1 μm^2 inside a single grain and collected through a 100 $\times$ objective. The laser power was kept below 1 mW to avoid in-beam sample annealing. The estimated probed depth of

~2.3 µm for a photon energy of 2.33 eV by Raman spectroscopy in CeO_2 [*Costantini, 2019a*] is marked by a vertical dotted line in the depth profiles (Fig. 1).

III. RESULTS AND DATA ANALYSIS

III.1 X-ray diffraction data

The XRD powder patterns are displayed for the various virgin samples (Fig. 2 a) and the lattice parameter deduced from the (111) reflection is plotted versus the Gd_2O_3 content (Fig. 2 b). The lattice parameter is increasing versus the Gd_2O_3 content, in agreement with the literature data [*Mogensen, 2000; Ruiz-Trejo, 2013*]. A clear broadening of the (111) Bragg peak is found with the increasing Gd content (Fig. 2 b).

III.2 Diffuse UV-visible reflectivity data

Diffuse reflectivity spectra versus photon energy ($\hbar\omega$) are shown for virgin and irradiated samples up to 6 eV (Figs. 3 a-b-c) corrected for the background and reference blank. The reflectance was set to zero for $\hbar\omega$ ~6 eV, corresponding to transitions above the 2p–5d band gap [*Wuilloud, 1974*]. The large variations of reflectance below the 2p–4f optical gap at ~3 eV are partly attributed to the difference in the surface state of samples, e. g. polishing after heat treatment. Therefore, only the relative evolutions of spectra are considered and not in absolute values.

The spectra were treated with the Kubelka-Munk (K-M) function or re-emission factor (F) devised for thick samples in which self-absorption and scattering are significant (Figs. 4 a-b-c) [*Escobedo Morales, 2007; Nowak, 2009; Lopez, 2012*]:

$$F(\hbar\omega) = \frac{[1-R(\hbar\omega)]^2}{2R(\hbar\omega)} = \frac{\alpha(\hbar\omega)}{S} \qquad (1)$$

where R is the reflectance, α is the extinction coefficient, and S is the scattering factor. This function is relevant for the case of a two-layer sample with an irradiated zone of ~1 to 4 µm and non-irradiated material underneath. In this approximation, the reflection and scattering by the rear side of the sample is neglected.

The absorption edge including band tailing is fitted by the equation deduced from the photon energy dependence of α [*Dow, 1972; Cody, 1992; Johnson, 1995; Beaudoin, 1997*]:

$$F = F_0 + K\exp\left(\frac{E_G-\hbar\omega}{E_U}\right) \qquad (2)$$

where E_G is the band gap energy, E_U is the Urbach edge energy, and K is a constant taken as 1. No assumption is made on the type of optical gap either direct or indirect. The dispersion of reflectance data below ~3 eV (Figs. 3 a-b-c) has no impact on this analysis of the fundamental absorption edge, since it gives only a small offset value on the F-scale (Figs. 4 a-b-c).

The plots of E_G and E_U versus fluence (φ) (Fig. 4, insets) are showing the decrease of E_G and increase of E_U to asymptotic values, regardless of the Gd content, that are least-square fitted with the following equations:

$$E_G = E_{G,\infty} + (E_{G,0} - E_{G,\infty})\, e^{-\sigma \varphi} \quad (3)$$

$$E_U = E_{U,0} + (E_{U,\infty} - E_{U,0})\,(1 - e^{-\sigma' \varphi}) \quad (4)$$

where $E_{G,0}$ and $E_{U,0}$ and are the initial values and $E_{G,\infty}$ and $E_{U,\infty}$ are the asymptotic values. The decay of E_G according to Eq. (3) and rise to saturation of E_U according to Eq. (4) yield the cross sections of σ and σ', respectively (Table 2). Similar $E_{G,0}$ and $E_{U,0}$ values are found for the virgin samples (Table 2). The asymptotic values ($E_{G,\infty}$) of E_G are similar, regardless of the Gd content, whereas the asymptotic values ($E_{U,\infty}$) of E_U are similar for 1 mol% and 5 mol% Gd_2O_3, but larger for undoped CeO_2 (Table 2).

Absorption bands centered at ~5 eV and 6 eV are found for all virgin and irradiated samples (tagged with arrows in Figs. 4 a-b-c) above the 2p–4f optical gap at ~3.2 eV (marked by dashed vertical lines in Figs. 4 a-b-c). A small absorption band at ~1.5 eV is also found for the irradiated undoped CeO_2 sample, and bands at ~2 eV for virgin and irradiated samples with 1 mol% Gd_2O_3 (tagged with arrows in Figs. 3 a-b). Those bands seem to be smeared out for 5 mol% Gd_2O_3 (Fig. 2 c).The absorption bands above the optical gap are well expanded in the plot of the F-factor which is proportional to α (Figs. 4 a-b-c). They are fitted with three Gaussian profiles for all kinds of samples (Figs. 4 a-b-c). All fitted parameters such as band centers and respective FWHMs deduced from the standard deviations are listed for the various fluences (Table 2). Similar band centers and band widths are obtained for all samples, regardless of the Gd-content.

III.3 Raman spectroscopy data

Raman spectra are displayed for the virgin samples (Fig. 5, on an expanded semi-log scale) and irradiated samples (Figs. 6 a-b-c). The sharp peak of the Raman-allowed *gerade* F_{2g} (or triply degenerate T_{2g}) mode at ~465 cm^{-1} and the five satellites at close Raman shifts of ~494, 512, 524, 537, and 555 cm^{-1} are found regardless of the Gd_2O_3 content (Fig. 5), like for undoped CeO_2 [*Costantini, 2017, 2019a*]. No significant shifts of the F_{2g} peak and its satellites are found as a function

of the Gd content (Fig. 5). Those satellites are not labelled on a theoretical standpoint, but they can be associated to the oxygen deficiency, with comparison to samples doped with RE^{3+} or Y^{3+} showing a broad band peaking at ~550-600 cm^{-1} which was assigned to intrinsic and extrinsic oxygen vacancies [*Nakajima, 1994*; *McBride, 1994, Dohčević-Mitrović, 2007, Kainbayev, 2020*]. Several overtones and second-order peaks are also recorded above 600 cm^{-1}, such as the broad bands peaking at ~667, 912, and 970 cm^{-1}.

Some lattice disorder is already present in the virgin sample for 5 mol% Gd_2O_3, as seen by the asymmetrical broadening of the F_{2g} peak and merging of satellite peaks (Fig. 5). Such asymmetrical broadening of the F_{2g} peak increasing with the Gd content was already reported for $Ce_{1-y}Gd_yO_{2-y/2}$ thin films for y = 0.1, 0.2, and 0.3 (i. e. 5, 10 and 15 mol% Gd_2O_3) [*Ruiz-Trejo, 2013*]. This is consistent with the clear broadening of the (111) Bragg peak in the XRD patterns (Fig. 2 b).

The extra band at ~250 cm^{-1} for 5 mol% Gd_2O_3 is also broadened and shifted with respect to the broad band peaking at ~230 cm^{-1} for the virgin undoped sample and the virgin sample for 1 mol% Gd_2O_3 (Fig. 5). The latter bands can be related to the otherwise forbidden acoustic mode (folded A_{1u} in the [ζζζ] direction) for null strain [*Buckeridge, 2013*] which can be become active owing to disorder [*Brodsky, 1978*]. The overtones at ~667, 912, and 970 cm^{-1} are also clearly broadened for 5 mol% Gd_2O_3 (Fig. 5). The IR-active *ungerade* optical modes of F_{1u}-TO at ~270 cm^{-1} and F_{1u}-LO at ~590 cm^{-1} [*Buckeridge, 2013*] are tagged to show the limits of the optical phonon range (Fig. 5). The peak at ~670 cm^{-1} is near the combination mode of the F_{2g} mode and disorder peak (A_{1u}-L) at ~230 cm^{-1}. The other two second-order peaks are close to the $2F_{2g}$ overtone.

No strong radiation damage is observed for all samples (Figs. 6 a-b-c), except for the decrease and small asymmetrical broadening of the F_{2g} peak intensity, in agreement with previous results for undoped CeO_2 after heavy ion irradiation [*Costantini, 2017, 2019a*]. The satellites and overtones are also decaying as well. The broad fluorescence background increasing with fluence is subtracted from the spectra for sake of clarity. The F_{2g} peak intensity (I) normalized to the virgin sample value (I_0) is plotted as a function of fluence for the three kinds of samples (Figs. 5 a-b-c, insets). Damage cross sections (Σ) are deduced from the least-square fits of the decay of (I/I_0) versus fluence [*Costantini, 2017, 2019a*] according to:

$$\left(\frac{I}{I_0}\right) = \left(\frac{I}{I_0}\right)_\infty + \left[1 - \left(\frac{I}{I_0}\right)_\infty\right] e^{-\Sigma \varphi} \qquad (5)$$

It is found that Σ is decreasing with the Gd content, regardless of the I_0 value (Table 2).

IV. DISCUSSION

IV.1 Raman spectroscopy data

No striking radiation effects are found for all sintered CeO_2 and (Ce, Gd)O_{2-x} samples, in agreement with previous results [*Costantini 2017, 2019a; Graham, 2018*], except for a decrease of the F_{2g} peak intensity and strong increase of the fluorescence background, especially for the largest fluences. No clear F_{2g} peak broadening due to irradiation is observed. A lower damage cross section (Σ) is deduced for 5 mol% Gd_2O_3 with respect to the other samples. This may arise from the initial disorder evidenced by the shouldering and broadening of the F_{2g} peak in the virgin and irradiated samples (Fig. 5), already found for (Ce, Gd)O_{2-x} thin films [*Ruiz-Trejo, 2013*]. As such, this disorder has nothing to do with the method of preparation by sintering. This is rather an intrinsic feature of Gd^{3+} doping, even though the lattice strain is weak, as mentioned above.

Regarding the radiation effects, unfortunately, *Tahara et al*. did not provide the cross sections corresponding to the lattice parameter expansion versus fluence, exhibiting a saturation behavior for 200-MeV Xe ion irradiation [*Tahara, 2011*]. Estimations of the damage cross sections (S) are deduced from the published lattice parameter data by *Tahara et al.* [*Tahara, 2011*] (Table 2). The damage cross section clearly increases for 10 mol% Gd_2O_3, but the value for 5 mol% Gd_2O_3 is close to the Σ value (Table 2). It is to be noted that the latter cross sections are much larger than the track cross sections measured by TEM [*Sonoda, 2006*] and STEM [*Takaki, 2016*] for these stopping power values [*Costantini, 2017*]. The lattice parameter increase ($\Delta a/a_0$) measured by XRD (by 0.2% in relative value at saturation for 10 mol%) is accompanied by an increase of the Ce–O and Ce–Ce interatomic distances (by 0.4-0.5% at saturation for 10 mol%) measured by XAFS at the Ce L3-edge and Gd L3-edge [*Tahara, 2012*]. The increase of disorder is also evidenced by the broadening of the (331) Bragg peak versus fluence which is about the same regardless of the Gd-content [*Tahara, 2011*]. The same cross section (S') is deduced from the plot of the FWHM versus fluence, regardless of the Gd-content (Table 2). It is close to the S value for 1 mol%. This is quite puzzling since the Bragg peaks should in principle reflect the increase of disorder for a larger Gd content.

Substitution of Gd^{3+} for Ce^{4+} induces an increase of the lattice parameter (a_0) as a function of the Gd-content (Fig. 1 b), since the ionic radius of Gd^{3+} is larger than that of Ce^{4+}, as explained in the introduction [*Mogensen, 2000; Ruiz-Trejo, 2013*]. The formation of Ce^{3+} ions also induces an increase of the unit cell constant [*Mogensen, 2000*]. In contrast, *Tahara et al.* have deduced a decrease of the lattice parameter from the (311) reflection as a function of the Gd content from a_0 ~5.408 Å for undoped CeO_2 with a saturation at a_0 ~5.406 Å for 10 mol% Gd_2O_3, but no broadening of the (331) Bragg peak by Gd doping [*Tahara, 2011*]. This is at variance with our XRD data for the virgin samples (Fig. 2 b) and with the literature data [*Mogensen, 2000; Ruiz-Trejo, 2013*].

Moreover, a decrease of the Ce–O and Gd–O interatomic distances versus Gd content was reported from XAS spectra at the Ce L3-edge and Gd L3-edge in powdered samples of $Ce_{1-y}Gd_yO_{2-y/2}$ for $0 \leq y \leq 0.3$ (i. e. up to 15 mol% Gd_2O_3) [*Ohashi, 1998*]. This was interpreted by the lattice relaxation around Ce and Gd atoms near the oxygen vacancies ($V_O^{\cdot\cdot}$) generated by charge compensation. It was concluded from XAS data that $(Gd_{Ce}' – V_O^{\cdot\cdot})^{\cdot}$ defect clusters are formed [*Ohashi, 1998*] in agreement with defect simulations [*Minervini, 1999*]. This is also in agreement with more recent *ab initio* DFT calculations showing that oxygen vacancies are the dominant point defects induced by trivalent RE doping [*Nakayama, 2009*]. As a result, the radiation effect on the lattice parameter is a complex outcome of point and extended defect formation which is not easily accounted for.

The discrepancies with results by *Tahara et al.* for the same range of Gd doping, but larger stopping power (S_e = 27.5 MeV μm^{-1}) [*Tahara, 2011, 2012*], are puzzling and need be addressed. As mentioned in the introduction, the various experimental techniques are probing the damage at different length scales. For instance, XRD yields information on the lattice disorder on a long-range scale, by including scattering of a large number of scattering centers. On the other hand, XAS is probing the atomic disorder on a very short range, i. e. few atomic distances, around the X-ray absorbing species, i. e. Gd^{3+} and Ce^{4+} ions in the present case. In contrast, Raman scattering provides information about the disorder at the level of bonds, i. e. the allowed F_{2g} mode corresponding to Ce–O centro-symmetric vibrations in the CeO_8 shells [*Nakajima, 1994*; *Ruiz-Trejo, 2013*]. This means that conflicting conclusions may arise from these results.

In the present Raman spectra, no significant broadening or downward shift of the F_{2g} peak are found with ion fluence, as expected from the accumulation of oxygen vacancies and increase of lattice parameter [*McBride, 1994; Kainbayev, 2020; Schmitt, 2020*], and increase of the Ce–O distance, reported by *Tahara et al.* [*Tahara, 2012*]. Moreover, the decay of the F_{2g} peak intensity for 5 mol% Gd_2O_3 samples is not enhanced at all with respect to the undoped CeO_2 samples, it is rather reduced. The impact of the lattice binding energy on the radiation damage claimed by *Tahara et al.* is however questionable. Moreover, the alleged increase of Ce–O and Ce–Ce interatomic distances and related volume swelling does not prove that the binding energy is lowered.

It is to be noted that Raman spectra only probe a depth of ~2.3 µm for $\hbar\omega$ = 2.33 eV [*Costantini, 2019a*]. Thus, the major contribution to the Raman spectra of undoped CeO_2 samples and for 5 mol% Gd_2O_3 derives from electronic excitations for the 12-MeV Ar ion irradiation (Fig. 1). In contrast, both nuclear collisions and electronic excitations contribute to the Raman spectra of samples with 1 mol% Gd_2O_3, for the 2.5-MeV Ar ion irradiation (Fig. 1). However, a similar Σ value is found for 1 mol% Gd_2O_3, even though the nuclear stopping power for 2.5 MeV is twice as large as for

the 12-MeV energy (Table 1). No clear effect of the large number of displaced C and O atoms for such high fluences (Table 1) is found on the Ce–O bonds and vibrations. There is no clear evidence of a contribution of nuclear collisions to the observed damage, but rather a major effect of electronic excitations. In this respect, the discrepancy with results of *Tahara et al.* [*Tahara, 2011, 2012*] may partly be accounted for by the larger electronic stopping power (S_e = 27.5 MeV μm^{-1}), as compared to the present values ($S_e \leq$ 6.6 MeV μm^{-1}), and the larger Gd_2O_3 content of 10 mol%.

IV.2 Diffuse UV-visible reflectivity data

IV.2.a. Optical absorption edge

Both nuclear collisions and electronic excitations contribute to the diffuse reflectivity spectra of all samples probing the whole thickness for both ion energies (Fig. 2). The UV-visible absorption and reflection spectra are known to probe the electronic structure of semiconductors or insulators [*Pankove, 1975*]. The band-gap energy deduced from the K-M plots (Eq. 1) may differ from the values inferred from standard optical transmission spectra [*Escobedo Morales, 2007; Nowak, 2009; Lopez, 2012*]. The E_G value of ~2.7 eV for virgin undoped CeO_2 is lower than the value ~3.2 eV deduced from the spectrum in the transmission mode for as-grown single crystals [*Costantini, 2016, 2018*]. There is definitely a contribution of scattering at the interface between the irradiated zone and the underlying virgin substrate which may induce a wrong estimation of the band-gap energy using various equations [*Lopez, 2012*]. No clear change in E_G of virgin samples is found for the present low Gd contents ($y \leq 0.1$), as compared to the case of thin films of $Ce_{1-y}Gd_yO_{2-y/2}$ showing a small decrease of the indirect band-gap from 3.33 eV for y = 0.1 (i. e. 5 mol% Gd_2O_3) to 3.31 eV for y = 0.2 (i. e. 10 mol% Gd_2O_3), and 3.28 eV for y = 0.3 (i. e. 15 mol% Gd_2O_3) [*Ruiz-Trejo, 2013*]. Moreover, there is no clear effect on band tailing in the virgin samples for such a low Gd content, in contrast to Ni-doped samples showing a clear indirect band-gap reduction from ~3 eV to ~2.4 eV, and increase of the Urbach energy from ~0.15 eV to ~0.7 eV for 10 Ni at% substitution [*Tiwari, 2020*]. This is likely due to the difference in lattice strain induced by the Ni^{2+} and Gd^{3+} substitutions.

Anyway, there is a decrease in band-gap energy and increase in Urbach energy after irradiation which is likely due to point defect accumulation, regardless of the Gd_2O_3 content, even though there is no strong lattice disorder, as seen by the Raman spectra. Reflectivity spectra are consistent with the previous results on electron-irradiated CeO_2 single crystals showing an extra absorption tail [*Costantini, 2016, 2018*] near the 2p–4f band-gap at ~3.2 eV [*Crnjak Orel, 1994; Guo, 1995; Oh, 2012*]. A surprising larger increase of E_U is deduced for undoped CeO_2 with respect to the Gd-doped samples. It is larger than the value for 5 mol% Gd_2O_3 sample which was irradiated exactly in the same conditions with 12-MeV Ar ions. However, the asymptotic values of E_G are similar for all

irradiated samples (Table 2). As a result, band tailing due to the accumulation of point defects seems to be stronger in undoped ceria than in the Gd-substituted samples.

Similar damage cross sections σ and σ' are obtained for undoped CeO_2 and for 5 mol% Gd_2O_3 (Table 2) after the same 12-MeV Ar ion irradiation. Those two cross sections for the electronic stopping power of S_e = 6.6 MeV μm^{-1} are very close (Table 1). They are also close to the cross section for the growth of the 4f $\rightarrow$ 5d absorption bands related to Ce^{3+} formation in undoped CeO_2 for S_e = 4.8 MeV μm^{-1} [*Costantini, 2019b*]. A saturation of the latter cross section was found for values of S_e > 6 MeV μm^{-1}. This is consistent with an electronic excitation process for this large electronic stopping power, rather than a nuclear-collision process, even though displacement damage is also produced in all samples (Fig. 1).

Moreover, similar values of the damage cross sections (σ' ~1x10^{-13} cm^2) for the two ion energies (Table 2) are obtained for the Urbach energy saturation, regardless of the Gd_2O_3 content. This hints again to the same damage process induced by electronic excitations, responsible for band tailing in those materials. The σ and σ' values are consistent with the Σ values deduced from Raman spectra (Table 2). However, as already mentioned above, they are much larger than the track cross sections deduced by TEM [*Sonoda,* 2006], and even more by STEM [*Takaki, 2016*], for undoped ceria [*Costantini, 2017, 2019b*].

IV.2.b. Absorption bands

The three broad absorption bands centered at ~4.6 eV, ~5 eV and ~6 eV (tagged with arrows in Figs. 3 a-b-c) above the 2p–4f optical gap for all virgin and irradiated samples, regardless of the Gd-content, correspond to the 2p $\rightarrow$ 5d CT bands, previously found for undoped CeO_2 sinters [*Costantini, 2019b*]. The band at ~1.5 eV is only found for the undoped CeO_2 samples and the bands at ~2.0-2.2 eV are found for 1 mol% Gd_2O_3 (tagged with arrows in Figs. 3 a-b), below the 2p–4f optical gap. Absorption bands at 1.2 eV and 2.2 eV were actually assigned to 4f $\rightarrow$ 5d transitions due to Ce^{3+} formation in undoped CeO_2 [*Costantini, 2019b*]. However, the present reflectivity spectra do not give any evidence of the other band centered at 2.8 eV which was also assigned to 4f $\rightarrow$ 5d transitions [*Costantini, 2019b*]. Those bands below the 2p–4f optical gap are not appearing for 5 mol% Gd_2O_3 (Fig. 3 c). It looks like the Ce^{3+} formation is impeded by increasing the amount of Gd^{3+} ions.

Guo et al. have reported absorption bands at 255 nm (~4.85 eV), 285 nm (~4.35 eV) and 340 nm (~3.65 eV) in the UV-visible reflectivity spectra of undoped CeO_2 and rare-earth doped CeO_2 [*Guo, 2010*]. The assignment of the first band at ~4.8 eV to an $O^{2-} \rightarrow Ce^{3+}$ (2p $\rightarrow$ 4f) CT band is not consistent with the mid-gap position of the empty $4f^0$ level of Ce^{4+} deduced from resonant Raman

scattering [*Kraynis, 2019*] and corresponding to the 2p–4f optical gap at ~3.2 eV [*Crnjak Orel, 1994; Guo, 1995; Oh, 2012; Schmitt, 2020*]: it is rather a 2p → 5d CT band. Moreover, it is not consistent with the position of the occupied $4f^1$ level of Ce^{3+} which is lying even lower in energy, at ~2 eV above the top of the 2p valence band [*Castleton, 2019*]. The two latter bands at ~4.3 eV and ~3.5 eV were assigned to $O^{2-} \rightarrow Ce^{4+}$ (2p → 5d) CT and inter-band transitions, respectively. *Guo et al.* claimed that the absorption in the UV range (> 3 eV) is enhanced by the Gd^{3+} substitution [*Guo, 2010*]. We cannot confirm such conclusions from the present data showing strong bands at ~4.6 eV, ~5 eV and ~6 eV, regardless of the Gd content (Figs. 4 a-b-c), in agreement with precious diffuse reflectivity data on undoped CeO_2 [*Costantini, 2019b*]. Moreover, it is rather difficult to explain the impact of Gd^{3+} substitution on the 2p → 5d CT bands, corresponding to transitions between extended states of the valence band and conduction band, since the charge-compensated oxygen vacancies generate deep levels in the 2p–5d band gap, but not shallow levels [*Costantini, 2020*].

IV.3. Analysis of defect formation

It must be borne in mind that there is a complex charge balance in ($Ce_{1-y}Gd_yO_{2-y/2}$) since the oxygen deficiency is mainly fixed by the Gd^{3+} content [*Mogensen, 2000; Coduri, 2018*], producing oxygen vacancies ($V_O^{\cdot\cdot}$) by charge compensation [*Minervini, 1999; Nakayama, 2009*]. One oxygen vacancy with the 2+ charge is formed for every two Gd^{3+} as found from EXAFS data [*Ohashi, 1998*] in the second or third neighbor sites [*Minervini, 1999*]. The binding energy of an oxygen vacancy to the substitutional trivalent cations is strongly dependent on the cation size [*Minervini, 1999*]. The binding energy of RE^{3+} ions to $V_O^{\cdot\cdot}$ shows a minimum for Gd^{3+} in the rare-earth series [*Minervini, 1999*].

In a first approximation, it can be assumed that this charge equilibrium is not changed by oxygen or cerium Frenkel-pair accumulation produced by nuclear collisions. Electronic excitations can induce Ce^{3+} ions by electron trapping on Ce^{4+} ions, and a Ce^{3+}/Ce^{4+}equilibrium is generated in steady state conditions, as for undoped CeO_2 [*Costantini, 2019b*]. A stronger effect for 12-MeV Ar irradiation is expected on the reflectivity spectra and Ce^{3+} formation, owing to the higher electronic stopping power. Accordingly, the band-gap decrease for undoped CeO_2 samples and for 5 mol% Gd_2O_3 is similar (Table 2). This is consistent with a process induced by electronic excitations, as mentioned above. Yet, the Urbach-energy increase is larger for undoped samples than for both Gd-doped samples (Table 2). This means that the number of point defects induced by the electronic excitations, such as Ce^{3+} ions, is likely higher for the undoped samples. However, no clear and direct evidence of a decrease of Ce^{3+} ions is found for the irradiated Gd-doped samples, except for the absence of absorption bands below the 2p–4f optical gap. It is liable to think that Gd^{3+} ions (and the native

oxygen vacancies with a 2+ charge state) would change the Ce^{3+}/Ce^{4+} redox equilibrium by fixing the oxygen deficiency and reducing the number of Ce^{3+} ions.

Several equilibria can be written for the various charged species (Ce^{4+}, Ce^{3+}, Gd^{3+}, $V_O^{\cdot\cdot}$) assuming electronic excitation processes and no thermal reduction. For virgin undoped samples, the condition of electro-neutrality imposes that the fractional site occupancy of intrinsic oxygen vacancies ($[V_{\ddot{O},int}]$) resulting from reduction, in the thermal treatment during sintering, is given by [*Schmitt, 2020*]:

$$[V_{\ddot{O},int}] = \frac{1}{4}\,[Ce'_{Ce}] \qquad (6)$$

For virgin doped samples, the condition of electro-neutrality also imposes that the concentration of total oxygen vacancies ($[V_{\ddot{O}}]$) is [*Schmitt, 2020*]:

$$[V_{\ddot{O}}] = [V_{\ddot{O},int}] + [V_{\ddot{O},ext}] = \frac{1}{4}\,[Ce'_{Ce}] + \frac{1}{4}\,[Gd'_{Ce}] \qquad (7)$$

where $V_{\ddot{O},ext}$ are the extrinsic oxygen vacancies induced by Gd^{3+} substitution for Ce^{4+}. For a low native non-stoichiometry, one gets: $[V_{\ddot{O}}] = \frac{1}{2}\,[Gd'_{Ce}]$ [*Mogensen, 2000; Coduri, 2018; Schmitt, 2020*]. This means that the non-stoichiometry is mainly fixed by the Gd content, for given oxygen partial pressures [*Mogensen, 2000*]. However, for dilute concentrations, oxygen vacancies are not isolated but trapped in $(V_{\ddot{O}} - Gd'_{Ce})^{\cdot}$ dimers [*Ohashi, 1998; Minervini, 1999; Schmitt, 2020*], which are polaronic states [*Keating, 2012; Zacherle, 2013; Castelton, 2019*], according to the equilibrium:

$$V_{\ddot{O}} + Gd'_{Ce} \leftrightarrow (V_{\ddot{O}} - Gd'_{Ce})^{\cdot} \qquad (8)$$

with the equilibrium constant K_{dimer}, according to mass-action law:

$$K_{dimer} = \frac{[V_{\ddot{O}} - Gd'_{Ce}]}{[V_{\ddot{O}}][Gd'_{Ce}]} \qquad (9)$$

The neutral $(Gd'_{Ce} - V_{\ddot{O}} - Gd'_{Ce})^{x}$ trimers may also be formed, according to the equilibrium [*Schmitt, 2020*]:

$$2\,Gd'_{Ce} + V_{\ddot{O}} \leftrightarrow (Gd'_{Ce} - V_{\ddot{O}} - Gd'_{Ce})^{x} \qquad (10)$$

with the equilibrium constant K_{trimer}:

$$K_{trimer} = \frac{[(Gd'_{Ce} - V_{\ddot{O}} - Gd'_{Ce})^{x}]}{[Gd'_{Ce}]^2[V_{\ddot{O}}]} \quad (11)$$

Similar equations can be written for the charged $(Ce^{x}_{Ce} - V_{\ddot{O}} - Gd'_{Ce})^{\cdot}$ trimers. However, in standard conditions, owing to the low cation mobility, the concentration of such trimers is quite low. Moreover, K_{trimer} is definitely lower than $K_{dimer,}$ for a given Gd content.

The behavior upon ion irradiation must be now considered, as discussed previously for undoped CeO_2 [*Costantini, 2019b*]. Electron-hole ($e' - h^{\cdot}$) pairs and Frenkel pairs are both generated by the impinging ions. The number of ($e' - h^{\cdot}$) pairs is proportional to the energy lost by electronic excitations and ionizations along the ion path [*Alig, 1975*], whereas the number of displaced atoms by nuclear collisions over the ion range is computed with the SRIM code (Table 1). Subsequent trapping of free electrons can occur on Ce^{4+} ions yielding Ce^{3+} ions, while free holes are trapped on Ce^{3+} giving back Ce^{4+} ions, with two respective capture cross sections [*Costantini, 2019b*]. A steady-state equilibrium is so generated by those two competing reactions.

Actually, CL spectra have shown that the trimers $(Ce^{x}_{Ce} - V_{\ddot{O}} - Ce'_{Ce})^{\cdot}$ and $(Ce^{x}_{Ce} - V_{\ddot{O}} - Ce^{x}_{Ce})^{\cdot\cdot}$ are induced in CeO_2 by elastic collisions under electron beam [*Costantini, 2020*]. The following in-beam Ce^{4+}/Ce^{3+} redox equilibrium is generated between these two kinds of F centers:

$$(Ce^{x}_{Ce} - V_{\ddot{O}} - Ce^{x}_{Ce})^{\cdot\cdot} + e' \leftrightarrow (Ce^{x}_{Ce} - V_{\ddot{O}} - Ce'_{Ce})^{\cdot} + h^{\cdot} \quad (12)$$

with the equilibrium constant K'_{trimer}, assuming that $[e'] = [h^{\cdot}]$ for the intrinsic case:

$$K'_{trimer} = \frac{[(Ce^{x}_{Ce} - V_{\ddot{O}} - Ce'_{Ce})^{\cdot}]}{[(Ce^{x}_{Ce} - V_{\ddot{O}} - Ce'_{Ce})^{\cdot\cdot}]} \quad (13)$$

We assume that the same kinds of point defects are formed in (Ce, Gd)O_{2-x}, like in CeO_2. Hence, the same equilibrium between both kinds of trimers is possible. The activation energy (ΔE) of such redox equilibrium is the energy difference between the corresponding electronic levels. In a first approximation, ΔE is the energy difference of ~1 eV between the occupied $4f^1$ level of Ce_{Ce}' below the empty $4f^0$ level of Ce_{Ce}^{x} [*Castelton, 2019*], and thus, for a constant oxygen potential:

$$K'_{trimer} = K'_{trimer,0} \exp(-\frac{\Delta E}{k_B T}) \quad (14)$$

where k_B is the Boltzmann's constant, and $K'_{trimer,0}$ is a pre-factor, depending on the oxygen potential, but independent of temperature. The equilibrium constant K'_{trimer} between both trimers may decrease if the $(Ce_{Ce}^{x} - V_{\ddot{O}} - Ce'_{Ce})^{\cdot}$ level is pushed down in the band gap. Actually, a downward shift of the $(Ce_{Ce}^{x} - V_{\ddot{O}} - Ce'_{Ce})^{\cdot}$ trimer level with respect to the Ce_{Ce}' level below the 2p–4f gap was deduced from CL data of electron-irradiated undoped ceria [*Costantini, 2020*]. Gd^{3+} substitution may alter the position of this level and increase the activation energy (ΔE). The decrease of Ce^{3+} ions trapped in trimers could account for the decrease of $E_{U,\infty}$ from 0.30 eV for undoped CeO_2 to 0.22 eV for 5 mol% Gd_2O_3, i. e. by ~27% (Table 2). For an increase of ΔE from 1.0 eV to 1.2 eV, a decrease of K'_{trimer} by ~20% is expected according to Eq. (14) for constant temperature and oxygen partial pressure. Such an electronic effect is not linked at all to lowering of the lattice binding energy [*Tahara, 2012*]. Yet, the low binding energy of $(V_{\ddot{O}} - Gd'_{Ce})^{\cdot}$ dimers [*Minervini, 1999*] might play a role on the defect equilibria and the condition of electro-neutrality as for virgin samples.

The evolution of ceria upon irradiation for larger Gd_2O_3 contents, is definitely an exciting topic hitherto not studied, i. e. for larger oxygen vacancy concentrations, whereby clustering is most likely. In particular, the behavior of Ce–Gd–O solid solutions in the miscibility gap of the phase diagram is a key issue.

V. CONCLUSIONS

We have studied the damage induced in sintered samples of undoped CeO_2 and (Ce, Gd)O_{2-x} (for 1 and 5 mol% Gd_2O_3) by 2.5-MeV Ar^{2+} and 12-MeV Ar^{4+} ion irradiations at room temperature. Raman spectra show that no amorphization is produced in all three kinds of samples up to high fluences (i. e. ~2 to 5x10^{14} cm^{-2}). However, the damage cross section seems to decrease with the Gd^{3+} content, as deduced from the decay of the main T_{2g} peak with ion fluence. Moreover, the diffuse UV-visible reflectivity spectra show that these irradiations cause band-gap shrinkage and band tailing that are increasing with fluence to a saturation. The increase of band tails is larger for the undoped ceria samples than for the Gd-substituted samples. The respective roles of nuclear collisions and electronic excitations in the damage process are discussed. The increase of Gd content seems to prevent the formation of Ce^{3+} ions by electronic excitation processes, thereby reducing the band tailing and damage.

ACKNOWLEDGMENTS: Authors are indebted to the ANDROMEDE facility staff (S. Della Negra, and I. Ribaud, IPN, Orsay)) for the Ar ion irradiations.

References

[*Adachi, 1998*] G. Adachi, and N. Imanaka, Chem. Rev. 98 (1998) 1479.

[*Alig, 1975*] R. C. Alig, and S. Bloom, Phys. Rev. Lett, 35 (1975) 1522.

[*Brodsky, 1978*] M. H. Brodsky, and M. Cardona, J. Non-Crystal. Solids 31 (1978) 81.

[*Castleton, 2019*] C.W.M. Castleton, A. Lee, and J. Kullgren, J. Phys. Chem. C 123 (2019) 5164.

[*Coduri, 2018*] M. Coduri, S. Checchia, M. Longhi, D. Ceresoli, and M. Scavini, Frontiers in Chemistry 6 (2018) 526.

[*Costantini, 2011*] J.-M. Costantini, F. Beuneu, S. Morrison-Smith, R. Devanathan, and W. J. Weber, J. Appl. Phys. 110 (2011) 123506.

[*Costantini, 2013*] J.-M. Costantini, F. Beuneu, and W. J. Weber, "*Radiation Damage in Cubic-Stabilized Zirconia and Ceria*", in "*Properties of Fluorite Structure Materials*", Eds. P. Vajda and J. M. Costantini (Nova Science Publishers, New York, 2013), pp. 127-152.

[*Costantini, 2016*] J.-M. Costantini, G. Lelong, M. Guillaumet, W. J. Weber, S. Takaki, and K. Yasuda, J. Phys.: Condens. Matter 28 (2016) 325901.

[*Costantini 2017*] J.-M. Costantini, S. Miro, G. Gutierrez, K. Yasuda, S. Takaki, N. Ishikawa, and M. Toulemonde, J. Appl. Phys. 122 (2017) 205901.

[*Costantini 2018*] J.-M. Costantini, L. Binet, N. Touati, G. Lelong, M. Guillaumet, and W. J. Weber, J. Appl. Phys. 123 (2018) 025901.

[*Costantini, 2019*] J.-M. Costantini, G. Lelong, M. Guillaumet, D. Gourier, S. Takaki, N. Ishikawa, H. Watanabe, and K. Yasuda, J. Appl. Phys. 126 (2019) 175902.

[*Costantini, 2020*] J.-M. Costantini, P. Seo, AKM S. I. Bhuian, K. Yasuda,T. Ogawa, and D. Gourier, J. Lumin. 226 (2020) 117379.

[*Crnjak Orel, 1994*] Z. Crnjak Orel, and B. Orel, Phys. Stat. Sol (b) 186 (1994) K33.

[*Devanathan, 2008*] R. Devanathan, and W. J. Weber, J. Mater. Res. 23 (2008) 593.

[*Devanathan, 2010*] R.Devanathan, L. Van Brutzel, A. Chartier, C. Guéneau, A. E. Mattsson, V. Tikare, T. Bartel, T. Besmann, M. Stane, and P. Van Uffele, Energy Environ. Sci. 3 (2010) 1406.

[*Dohčević-Mitrović, 2007*] Z. D. Dohčević-Mitrović, M. Radović, M. J. Šćepanović, M. U. Grujić-Brojčin, Z. V. Popović, B. M. Matović, and S. B. Bošković, Appl. Phys. Lett. 91 (2007) 203118.

[*Eyring, 1967*] L. Eyring, Advances in Chemistry 71 (1967) 67.

[*Graham, 2018*] J.T. Graham, Y. Zhang, and W.J. Weber, J. Nucl. Mater. 498 (2018) 400.

[*Guo, 1995*] S. Guo, H. Arwin, S. N. Jacobsen, K. Järendahl, and U. Helmersson, J. Appl. Phys. 77 (1995) 5369.

[*Guo, 2011*] M. Guo, J. Lu, Y. Wu, Y. Wang, and M. Luo, Langmuir 27 (2011) 3872.

[*Ishikawa, 2012*] N. Ishikawa, and K. Takegahara, Nucl. Instr. and Meth. B 272 (2012) 227.

[*Kainbayev, 2020*] N. Kainbayev, M. Sriubas, D. Virbuka, Z. Rutkuniene, K. Bockute, S. Bolegenova, and G. Laukaitis, Coatings 10 (2020) 432.

[*Keating, 2012*] P. R. L. Keating, D. O. Scanlon, B. J. Morgan, N. M. Galea, and G. W. Watson**,** J. Phys. Chem. C, 116 (2012) 2443.

[*Kraynis, 2019*] O. Kraynis, I. Lubomirsky, and T. Livneh, J. Phys. Chem. C 123 (2019) 24111.

[*Kvashnina, 2013*] K. O. Kvashnina, S. M. Butorin, P. Martin, and P. Glatzel, Phys. Rev. Lett. 111 (2013) 253002.

[*Matzke, 1996*] H. Matzke, Nucl. Instr. Meth. B 116 (1996) 121.

[*McBride, 1994*] R. McBride, K. C. Hass, B. D. Poindexter, and W. H. Weber, J. Appl. Phys. 76 (1994) 2435.

[*Minervini, 1999*] L. Minervini, M. O. Zacate, and R. W. grimes, Solid State Ion. 16 (1999) 339.

[*Mogensen, 2000*] M. Mogensen, D. Lybye, N. Bonanos, P. V. Hendriksen, and F. W. Poulsen, Sol. State Ion. 174 (2000) 279.

[*Nakayama, 2009*] M. Nakayama, and M. Martin, Phys. Chem. Chem. Phys. 11 (2009) 3241.

[*Nakajima, 1994*] A. Nakajima, A. Yoshihara, and M. Ishigame, Phys. Rev. B 50 (1994) 13297.

[*Oh, 2012*] T.S. Oh, Y.S. Tokpanov, Y. Hao, W. Jung, and S.M. Haile, J. Appl. Phys. 112 (2012) 103535.

[*Ohashi, 1998*] T. Ohashi, S. Yamazaki, T. Tokunaga, Y. Arita, T. Matsui, T. Harami, and K. Kobayashi, Sol. State Ion. 113 (1998) 559.

[*Pankove, 1975*] J. I. Pankove, "*Optical Processes in Semiconductors*" (Dover, New York, 1975).

[*Petit, 2010*] L. Petit, A. Svane, Z. Szotek, W. M. Temmerman, and G. M. Stocks, Phys. Rev. B 81 (2010) 045108.

[*Ruiz-Trejo, 2013*] E. Ruiz-Trejo, J. Phys. Chem Solids 74 (2013) 605.

[*Schmitt, 2020*] R. Schmitt, A. Nenning, O. Kraynis, R. Korobko, A. I. Frenkel, I. Lubomirsky, S. M. Hailef, and J. L. M. Rupp, Chem. Soc. Rev. 49 (2020) 554.

[*Shannon, 1976*] R. D. Shannon, Acta Cryst. A 32 (1976) 751.

[*Shi, 2016*] L. Shi, E. Vathone, V. Olson, M. Freyss, and R. Hayn, Phys. Rev. B 94 (2016) 115132.

[*Sonoda, 2006*] T. Sonoda, M. Kinoshita, N. Ishikawa, M. Sataka, Y. Chimi, and A. Iwase, Nucl. Instr. and Meth. B 250 (2006) 254.

[*Sun, 2012*] C. Sun, H. Li, and L. Chen, Energy Environ. Sci. 5 (2012) 8475.

[*Tahara, 2011*] Tahara et al., Nucl. Instr. and Meth. B 264 (2011) 886.

[*Tahara, 2012*] Tahara et al., Nucl. Instr. and Meth. B 277 (2012) 53.

[*Takaki, 2016*] S. Takaki, K. Yasuda, T. Yamamoto, S. Matsumura, and N. Ishikawa, Progress in Nucl. Energy 92 (2016) 306.

[*Tiwari, 2020*] S. Tiwari, G. Rathore, N. Patra, A. K. Yadav, D. Bhattacharya, S.N. Jha, C.M. Tseng, S.W. Liu, Sajal Biring, and S. Sen,

[*Tracy, 2015*] C. L. Tracy, M. Lang, J. M. Pray, F. Zhang, D. Popov, C. Park, C. Trautmann, M. Bender, D. Severin, V. A. Skuratov, R.C. Ewing, Nat. Commun. 6 (2015) 6133.

[*Vitova, 2017*] T. Vitova , I. Pidchenko , D. Fellhauer , P. S. Bagus, Y. Joly, T. Pruessmann, S. Bahl, E. Gonzalez-Robles , J. Rothe , M. Altmaier , M. A. Denecke, and H. Geckeis, Nature Commun. 8 (2017) 16053.

[*Weber, 1984*] W. J. Weber, Radiation Effects 83 (1984) 145.

[*Wuilloud, 1974*] E. Wuilloud, B. Delley, D. Schneider, and Y. Baer, Phys. Rev. Lett. 53 (1974) 202.

[*Yasunaga, 2008*] K. Yasunaga, K. Yasuda, S. Matsumura, and T. Sonoda, Nucl. Instr. and Meth. B 266 (2008) 2877.

[*Zacherle, 2013*] T. Zacherle, A. Schriever, R. A. de Souza, and M. Martin, Phys. Rev. B 93 (2013) 134104.

Table 1: Irradiation features of CeO_2 (mass density = 7.215 g cm^{-3}) with Ar ions of incident energy E computed with the SRIM-2013 code [*http://www.srim.org/*]: mean projected range (R_p) $\pm$ longitudinal range straggling (ΔR_p), electronic stopping power (S_e), and nuclear stopping power (S_n), total number of C and O atom displacements per ion (N_d), and total displacements per ion path length (dN_d/dx). Values of R_p and (ΔR_p) into brackets were obtained by the full cascade simulations.

E (MeV)	2.5	12
R_p (µm)	1.10 ± 0.26 (1.16 ± 0.26)	2.97 ± 0.35 (3.23 ± 0.35)
S_e (MeV μm^{-1})	2.7	6.6
S_n (keV μm^{-1})	$1.6x10^2$	51
S_e/S_n	17	129
N_d	4070	5470
(dN_d/dx) (μm^{-1})	$3.7x10^3$	$1.8x10^3$

Table 2: Fitted parameters for the undoped and Gd-doped CeO_2 samples: ion energy (E), damage cross sections for the band-gap energy (σ) and Urbach energy (σ'), asymptotic values for the band-gap energy ($E_{G,\infty}$) and Urbach energy ($E_{U,\infty}$), deduced from the diffuse UV-visible reflectivity spectra (Figs. 4 a-b-c, insets), damage cross sections (Σ) deduced from the decay of the F_{2g} peak intensity versus fluence in Raman spectra (Figs. 6 a-b-c, insets), and damage cross sections deduced from the plots of lattice parameter (S) and FWHM of the (331) reflection (S') versus fluence [*Tahara, 2011*].

Mol% Gd_2O_3	Ion	E (MeV)	σ (cm^2)	$E_{G,0}$ (eV)	$E_{G,\infty}$ (eV)	σ' (cm^2)	$E_{U,0}$ (eV)	$E_{U,\infty}$ (eV)	Σ (cm^2)	S (cm^2)	S' (cm^2)
0	Ar	12	8.0×10^{-14}	2.7	2.4	9.6×10^{-14}	0.145	0.30	1.2×10^{-12}		
1	Ar	2.5	5.3×10^{-13}	2.8	2.6	1.5×10^{-13}	0.145	0.25	5.1×10^{-13}	2.2×10^{-13}	2.3×10^{-13}
5	Ar	12	1.0×10^{-13}	3.0	2.5	1.2×10^{-13}	0.12	0.22	6.0×10^{-14}	7.3×10^{-14}	2.3×10^{-13}
10	Xe	200								8.4×10^{-13}	2.3×10^{-13}

Table 3: Fitted parameters of the absorption bands (Figs. 4 a-b-c): band centers and FWHMs deduced from the Gaussian fits.

Mol% Gd_2O_3	E (MeV)	Fluence (cm^{-2})	Band center-1 (eV)	FWHM-1 (eV)	Band center-2 (eV)	FWHM-2 (eV)	Band center-3 (eV)	FWHM-3 (eV)
0	12	0	4.6	0.59	5.1	0.59	6.0	0.82
		$3.0x10^{12}$	3.2	0.59	5.0	0.75	6.0	0.35
		$1.8x10^{13}$	4.6	0.47	5.1	0.59	6.0	0.35
		$2.1x10^{14}$	4.6	0.47	5.1	0.59	6.0	0.35
1	2.5	0	4.6	0.47	5.1	0.30	6.0	0.71
		$5.0x10^{12}$						
		$7.0x10^{13}$						
		$5.0x10^{14}$	4.6	0.47	5.1	0.30	6.0	0.47
5	12	0	4.6	0.59	5.0	0.35	5.9	0.40
		$6.0x10^{12}$	4.6	0.47	5.1	0.25	6.0	0.71
		$1.0x10^{13}$	4.6	0.59	5.1	0.25	6.2	0.59
		$2.1x10^{14}$	4.6	0.59	5.1	0.30	6.0	0.71

Figure 1: Depth profiles of the electronic stopping power (dashed curves) and nuclear collision damage profiles (dotted curves) for 2.5-MeV Ar and 12-MeV Ar ions in CeO_2 deduced from full cascade simulations with the SRIM-2013 code [*http://www.srim.org/*].

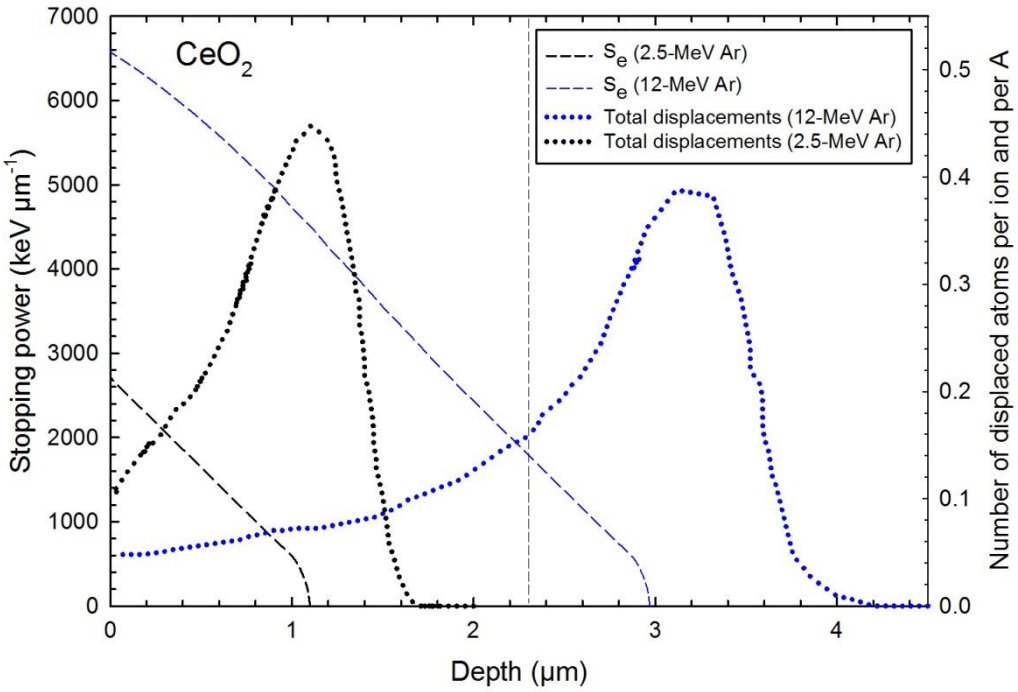

Figure 2: XRD powder patterns of the undoped and Gd-doped CeO_2 samples (a), FWHM of the (111) Bragg peak and lattice parameter deduced from the (111) reflection (b).

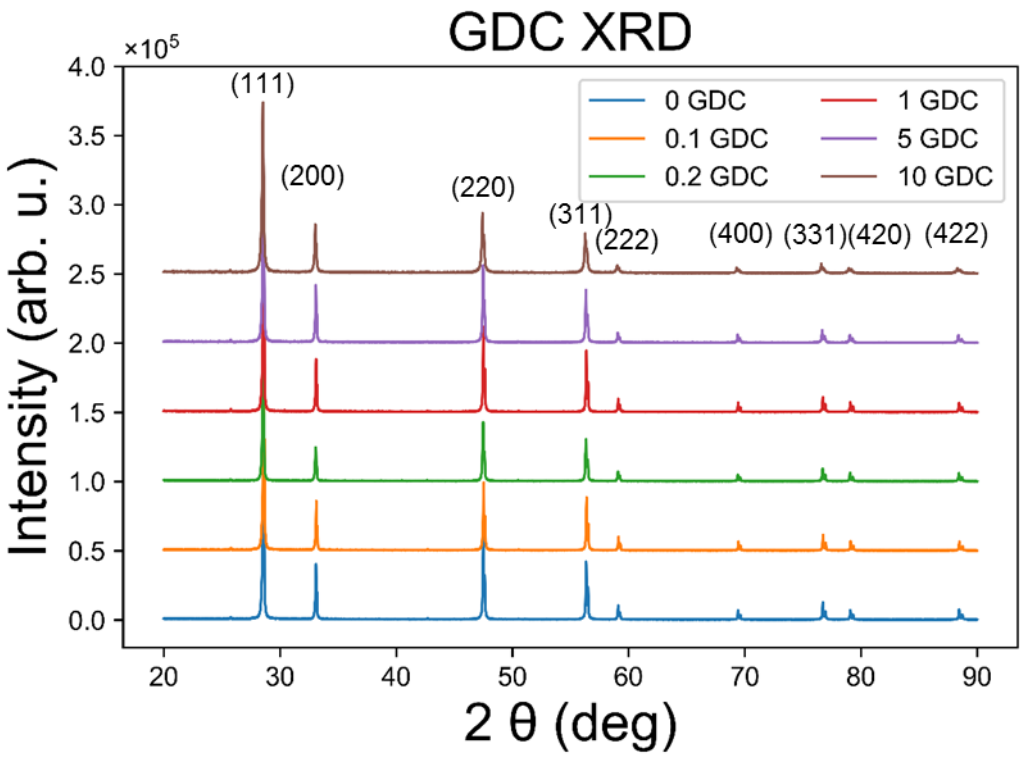

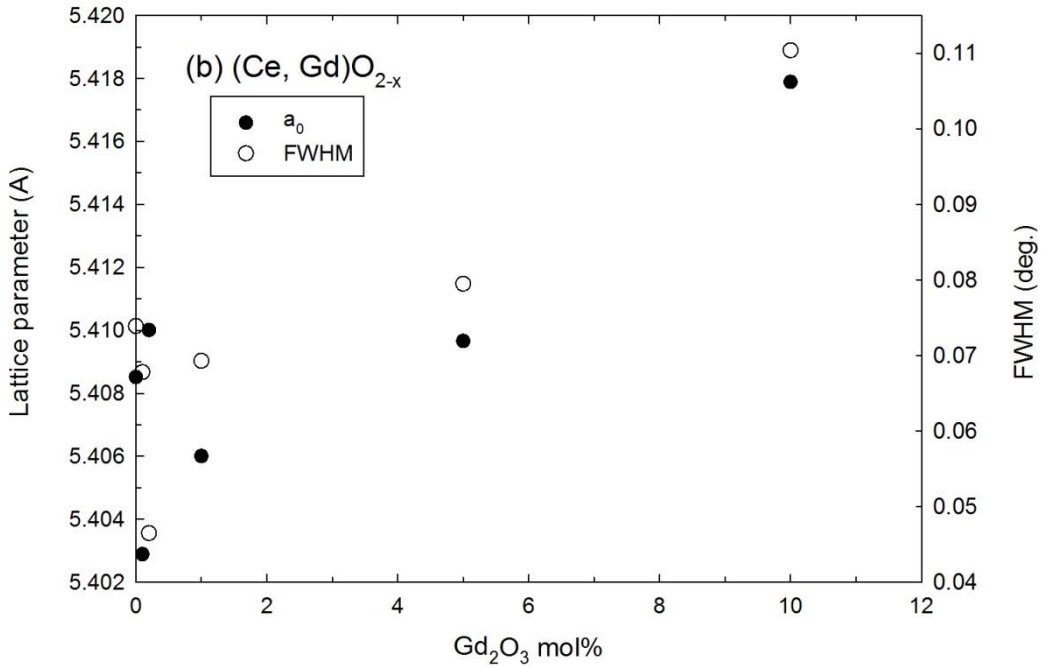

Figure 3: UV-visible diffuse reflectivity spectra of Ar-ion irradiated sintered samples of undoped CeO_2 (a), (Ce, Gd)O_2 for 1 mol% Gd_2O_3 (b), and (Ce, Gd)O_2 for 5 mol% Gd_2O_3 (c), corrected for background and reference sample. The 2p–4f optical gap is marked by dashed vertical lines. The absorption bands are tagged with arrows.

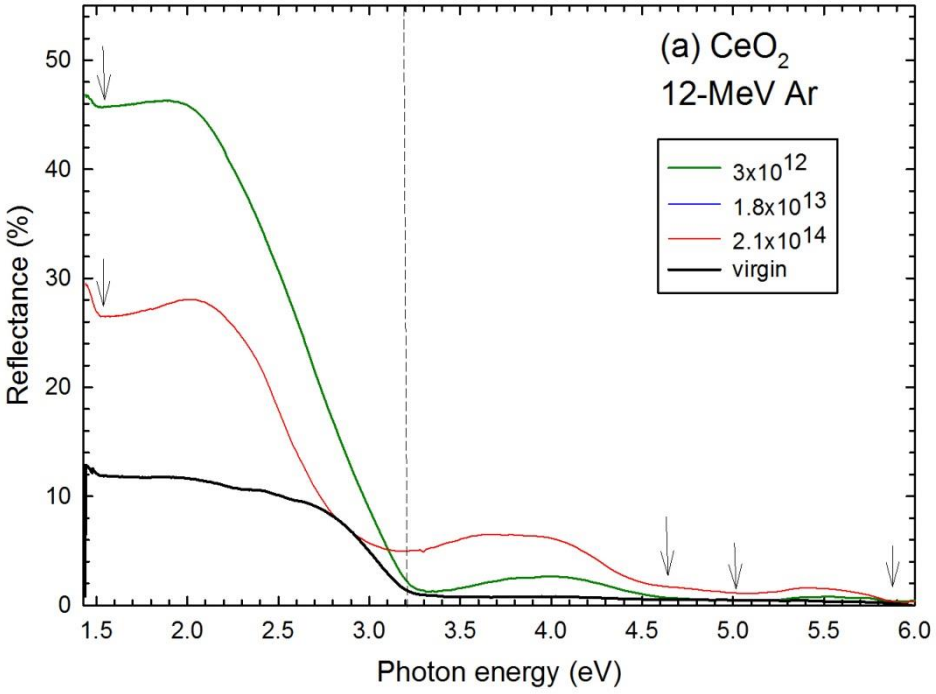

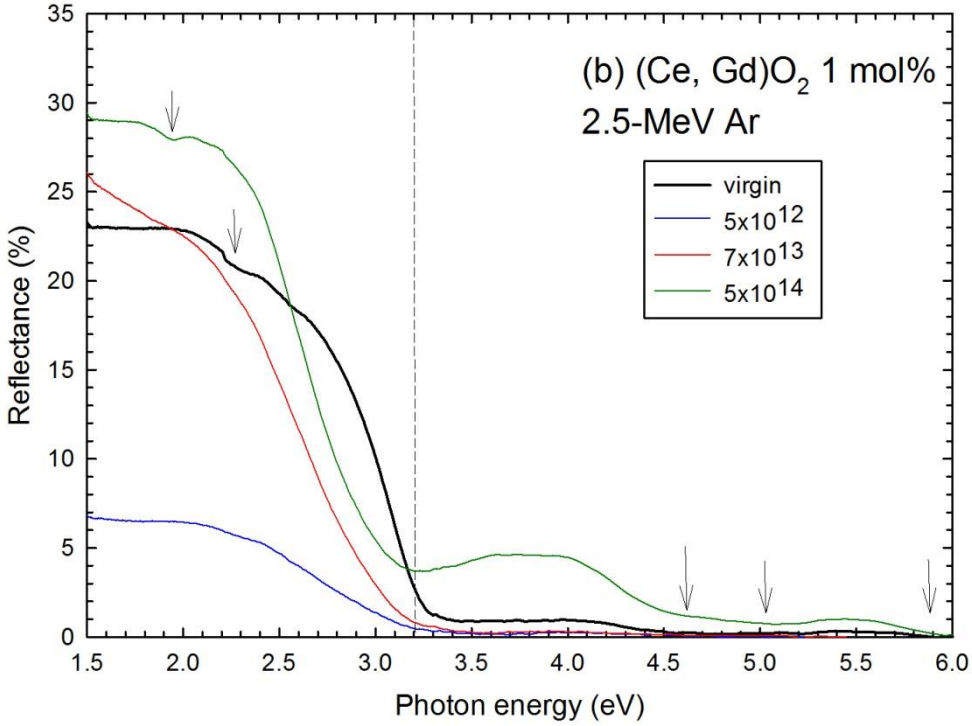
(b) (Ce, Gd)O2 1 mol%
2.5-MeV Ar
virgin
5x10^12
7x10^13
5x10^14
Reflectance (%)
Photon energy (eV)
0
5
10
15
20
25
30
35
1.5
2.0
2.5
3.0
3.5
4.0
4.5
5.0
5.5
6.0

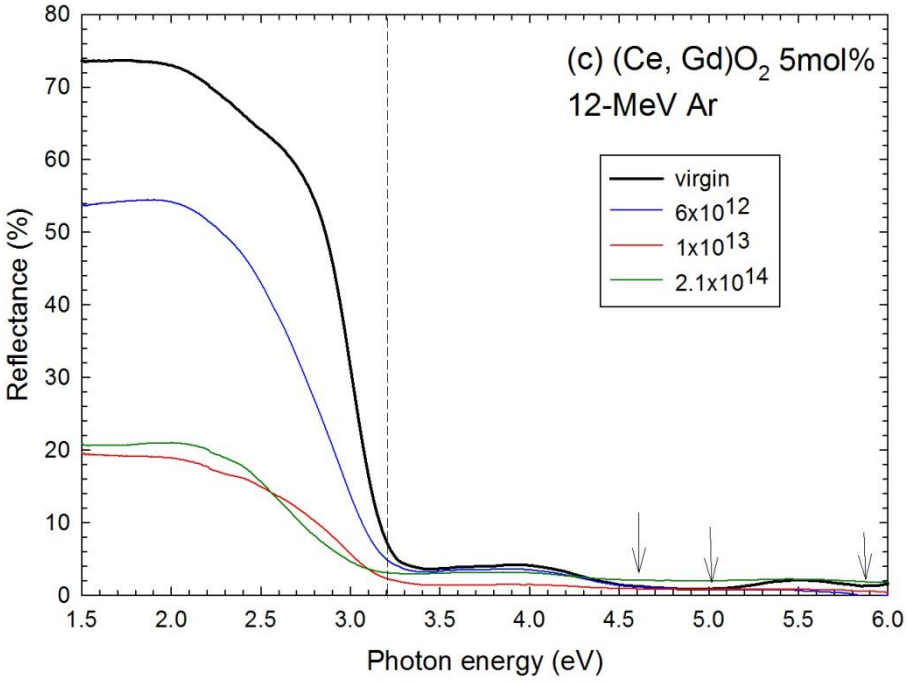
(c) (Ce, Gd)O2 5mol%
12-MeV Ar
virgin
6x10^12
1x10^13
2.1x10^14
Reflectance (%)
Photon energy (eV)
0
10
20
30
40
50
60
70
80
1.5
2.0
2.5
3.0
3.5
4.0
4.5
5.0
5.5
6.0

Figure 4: Re-emission factor (F) deduced by the Kubelka-Munk analysis (Eq. (1)) from the UV-visible diffuse reflectivity spectra of Ar-ion irradiated sintered samples of CeO_2 (a), (Ce, Gd)O_2 for 1 mol% Gd_2O_3 (b), and 5 mol% Gd_2O_3 (c). The dotted lines are fitted curves with Eq. (2) below the optical band gap and Gaussian profiles above band gap. Insets: band gap energy (E_G) and Urbach energy (E_U) versus fluence; solid curves are least-square fits with Eqs. (3)-(4).

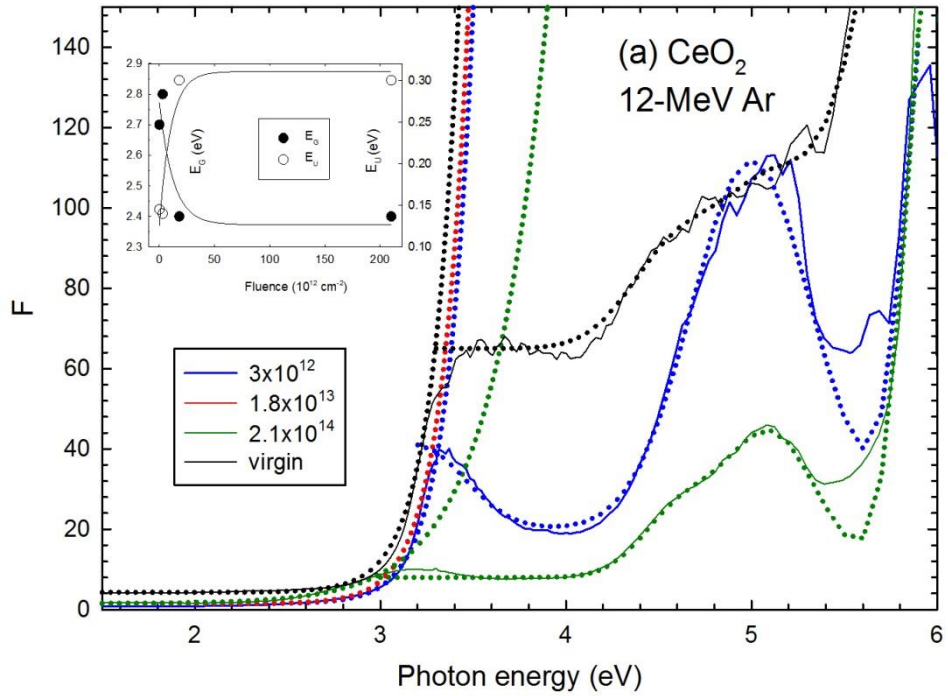

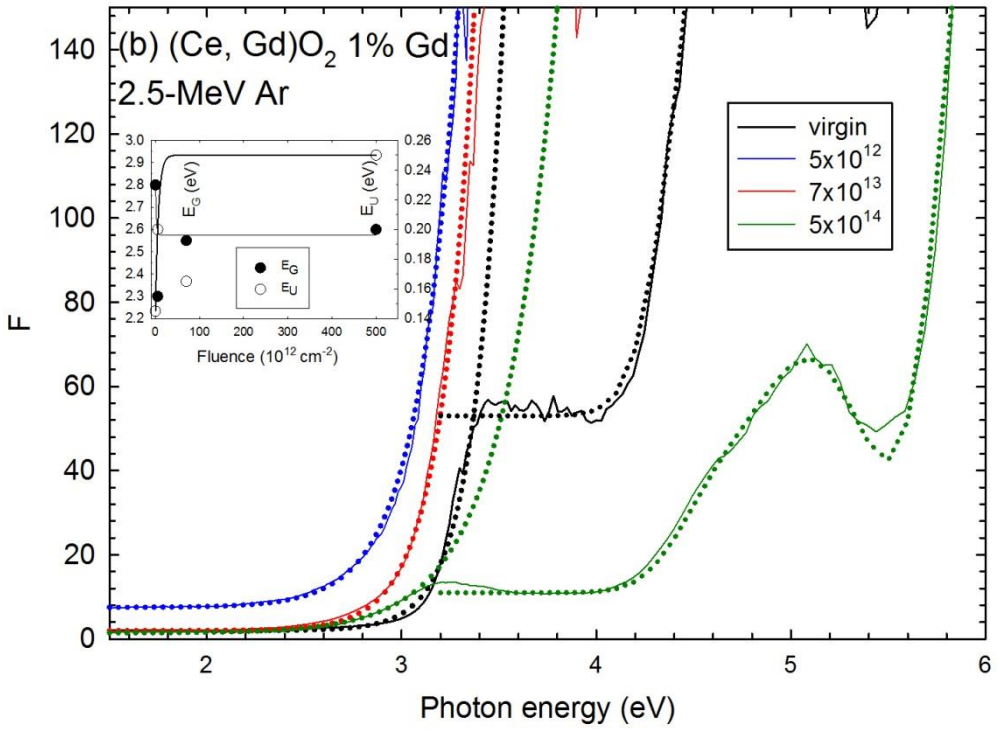
(b) (Ce, Gd)O2 1% Gd
2.5-MeV Ar
virgin
5x10^12
7x10^13
5x10^14
F
Photon energy (eV)
E_G (eV)
E_U (eV)
E_G
E_U
Fluence (10^12 cm^-2)

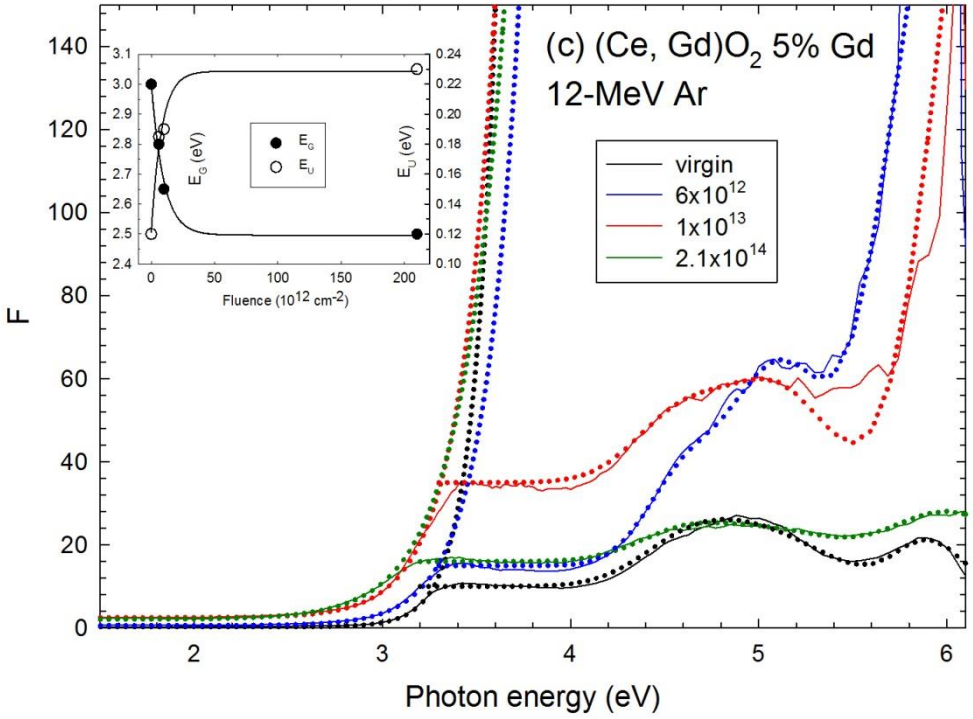
(c) (Ce, Gd)O2 5% Gd
12-MeV Ar
virgin
6x10^12
1x10^13
2.1x10^14
F
Photon energy (eV)
E_G (eV)
E_U (eV)
Fluence (10^12 cm^-2)

Figure 5: Micro-Raman spectra without background corrections of virgin sintered samples of CeO_2 (0 mol% Gd_2O_3), (Ce, Gd)O_2 for 1 mol% Gd_2O_3, and 5 mol% Gd_2O_3 (expanded on a semi-log scale). The spectra are shifted in intensity for sake of clarity.

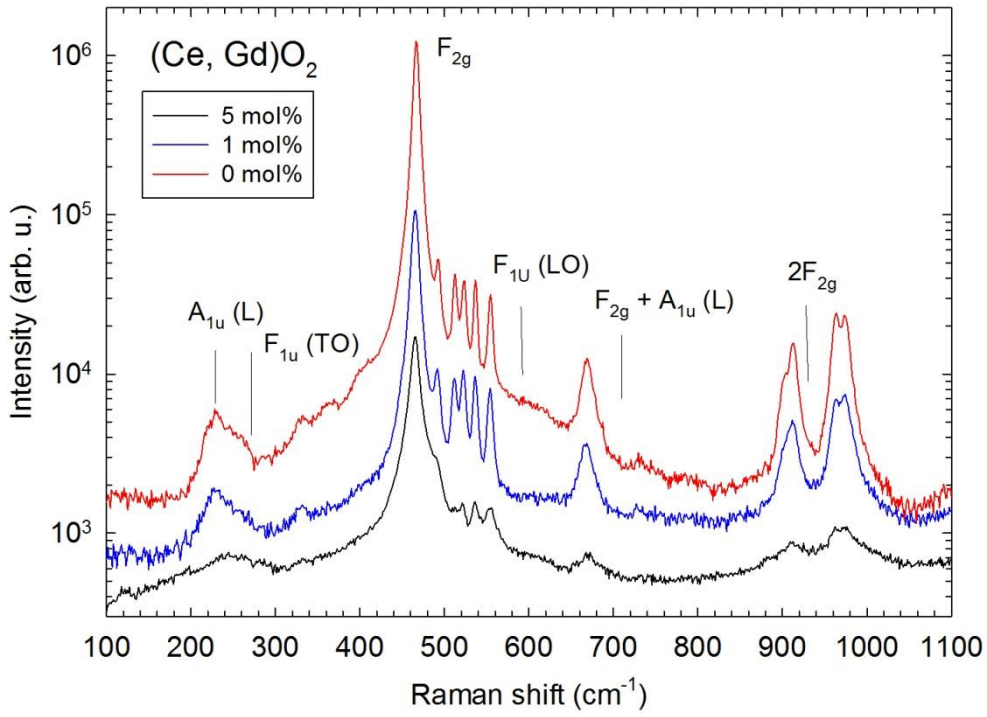

Figure 6: Micro-Raman spectra with fluorescence background corrections of Ar-ion irradiated sintered samples of CeO_2 (a), (Ce, Gd)O_2 for 1 mol% Gd_2O_3 (b), and 5 mol% Gd_2O_3 (c). Insets: Intensity of the T_{2g} peak (I) normalized to the virgin sample value (I_0) as a function of fluence.

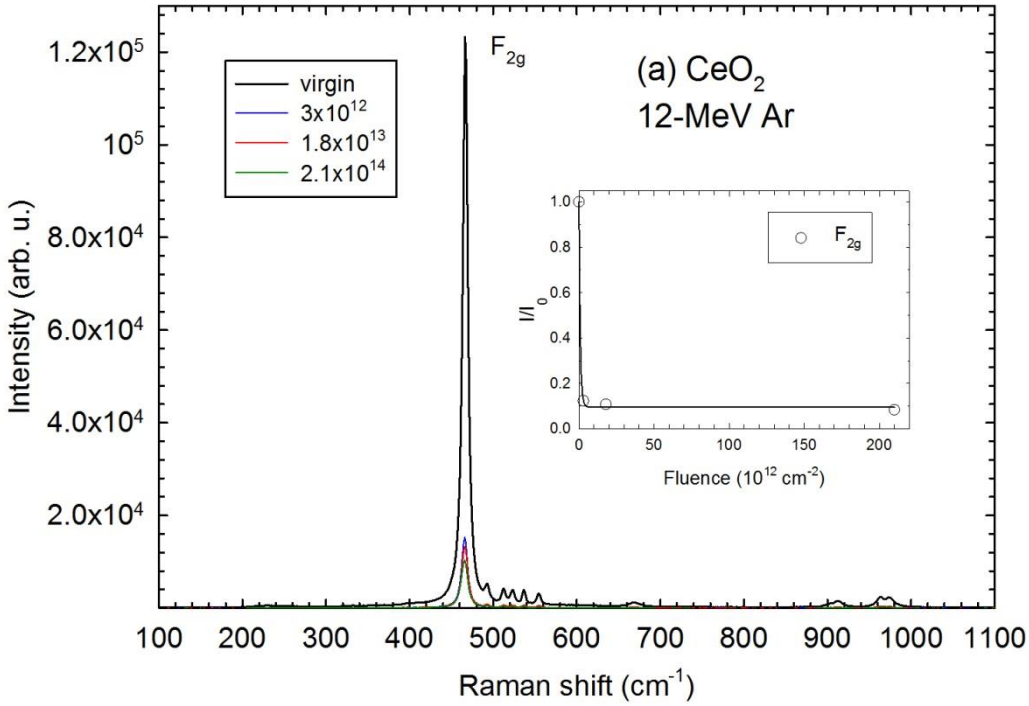

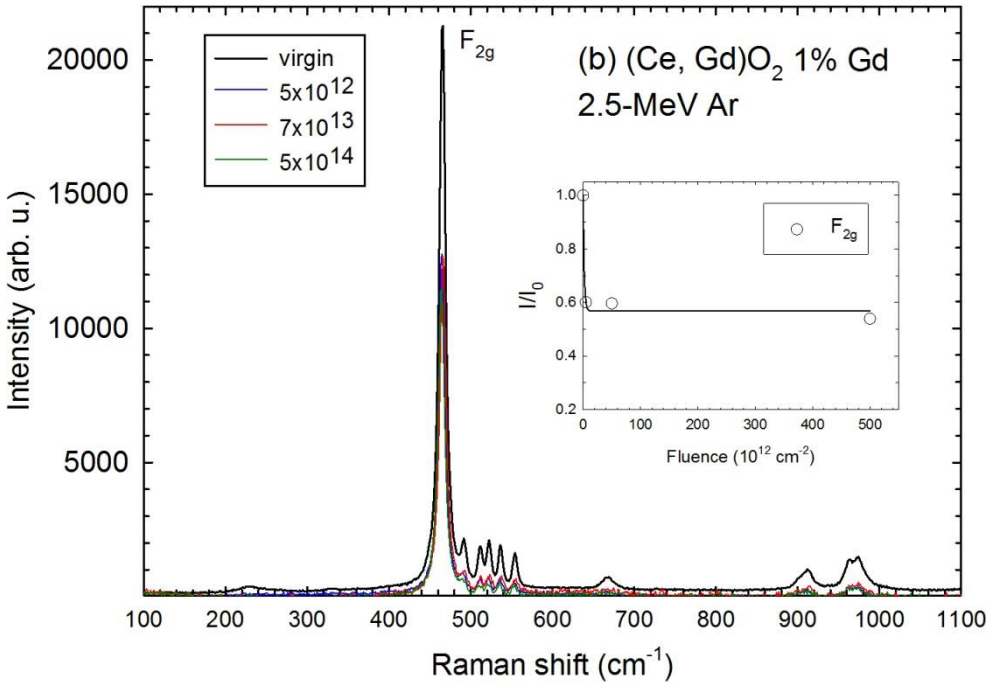
virgin
5x10^12
7x10^13
5x10^14
F2g
(b) (Ce, Gd)O2 1% Gd
2.5-MeV Ar
Intensity (arb. u.)
Raman shift (cm^-1)
I/I0
Fluence (10^12 cm^-2)

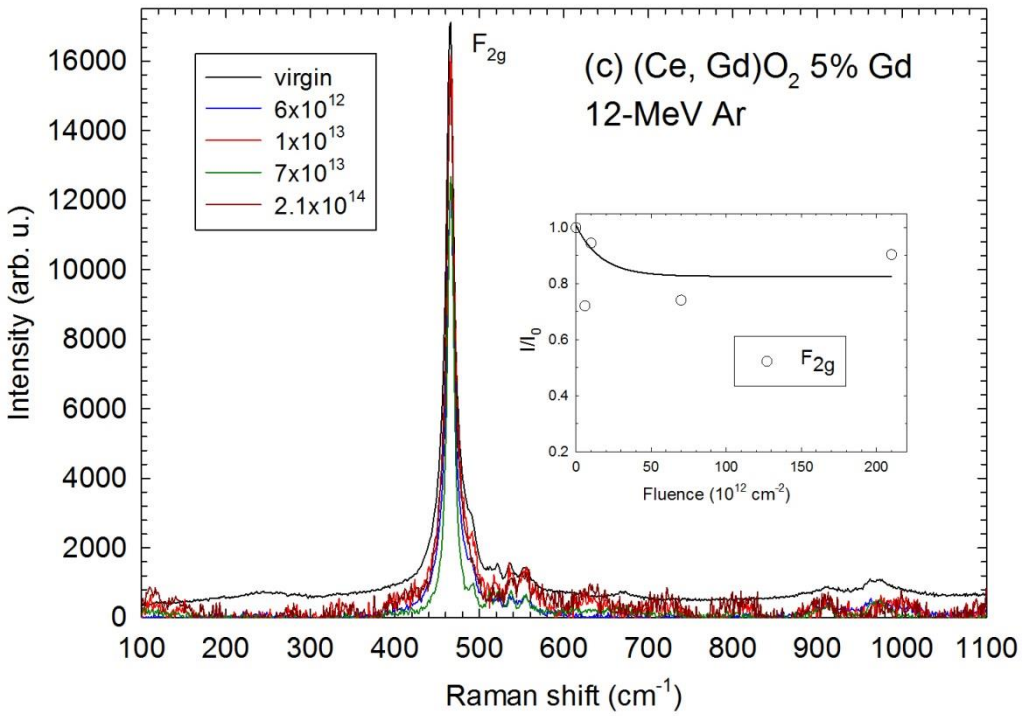
(c) (Ce, Gd)O2 5% Gd
12-MeV Ar
virgin
6x10^12
1x10^13
7x10^13
2.1x10^14
F2g
Intensity (arb. u.)
Raman shift (cm^-1)
I/I0
Fluence (10^12 cm^-2)